



# Non-singular Fast Terminal Sliding Mode Control Integrated with Proportional Multi-Resonant-Based Controller for Multifunctional Grid-Tied LCL-Filtered Inverter

Research paper

Amir Rabbani<sup>1</sup>, Mahla Dehghani<sup>1</sup>, Mohammad Mardaneh<sup>1</sup>, Ehsan Jamshidpour<sup>2,\*</sup>,  
Saeed Hasanvand<sup>3</sup>

<sup>1</sup>Department of Electrical Engineering, Shiraz University of Technology, Shiraz, Iran

<sup>2</sup>Université de Lorraine, Group of Research in Electrical Engineering of Nancy (GREEN), Nancy F54000, France

<sup>3</sup>Department of Electrical Engineering, Firouzabad Higher Education Center, Shiraz University of Technology, Shiraz, Iran

Received: 26 February, 2025; Received in the revised form: 19 May, 2025; Accepted: 03 July, 2025

**Abstract:** The growing utilisation of non-linear loads poses significant challenges to power quality in electrical grids. Non-linear loads, such as three-phase diode rectifiers, produce substantial harmonics, necessitating effective control methods to mitigate harmonic distortions. The implementation of active power filters (APF) offers significant potential for enhancing harmonic compensation performance. Accordingly, this research introduces a non-singular fast terminal sliding mode controller (NFTSMC) integrated with proportional multi-resonant (PMR) based control for a three-phase APF. The primary objective of this approach is to achieve rapid and precise tracking of reference currents while simultaneously injecting the desired currents into the electrical grid. Furthermore, to reduce harmonics generated by high-switching-frequency inverters, incorporating an LCL filter with an active damping strategy is essential. The PMR controller generates capacitor voltage references, ensuring zero steady-state error in the grid current and facilitating the implementation of the active damping method. Simulation results demonstrate the ordinary sliding mode controller (SMC) by achieving significantly lower total harmonic distortion (THD). Additionally, it exhibits superior dynamic response and robustness presence of uncertainties.

**Keywords:** active power filter • grid-tied inverter • LCL filter • PMR control VSI • non-singular fast terminal sliding mode controller

## 1. Introduction

The utilisation of voltage source inverters (VSIs) in grid-tied inverter (GTI) applications has become prevalent, driven by the increasing demand for sustainable energy sources. However, the presence of harmonic currents poses a threat to the efficacy of energy generation, transmission and utilisation. To address these issues, an advanced power electronic device known as an active power filter (APF) has been developed to generate compensating currents to mitigate the harmful effects of harmonic currents on the electric power system (Dehghani et al., 2020; Trinh and Lee, 2012).

Regarding APF, the primary objective of the control algorithm is to determine the reference compensation currents that are subsequently introduced into the grid at the point of APF connection (Maciążek, 2022). In an optimal scenario, the source current transforms into a sinusoidal active current while all adverse components are confined within the APF-load circuit. The high level of dynamics necessitated by this process typically entails

\* Email: Ehsan.jamshidpour@univ-lorraine.fr

time-domain simulation (Bosch et al., 2017; Sozanski and Szczesniak, 2023), although frequency-domain control algorithms can also be employed (Alali et al., 2019; Lou et al., 2022).

To meet required standards and establish sinusoidal currents between the inverter and the grid, implementing a filter is essential to mitigate the effects of PWM (Pulse Width Modulation) switching harmonics (Lou et al., 2022, IEEE Std 519-1992). Compared to L filter, LCL filter offers numerous advantages, including superior attenuation capabilities at lower switching frequencies due to their smaller inductance size (Mondal and Karuppaswamy, 2024; Satpathy and De, 2024; Zheng et al., 2018). However, LCL filters present inherent complexities from a control perspective. Resonance issues between filter components can introduce complex conjugate poles, potentially compromising system stability. Therefore, identifying an appropriate control strategy to ensure desirable system dynamics is critical.

To address resonance issues in the LCL filter, two general approaches have been employed: passive damping and active damping. Passive damping places low-value resistors within the LCL filter, a straightforward but less efficient solution (Liu et al., 2019). In contrast, active damping utilises virtual resistors and requires sensors for voltage or current measurement. Although active damping is more reliable than passive damping, it becomes unstable due to grid parameters variations and fluctuating resonance frequencies (Huang et al., 2023; Kolek and Firlit, 2021; Lorzadeh et al., 2016).

Different current control techniques utilising harmonic extraction as input demonstrate distinct approaches, each with its own advantages and limitations. The selection of an appropriate technique depends on factors such as the load's characteristics, robustness and ease of implementation.

Hou et al. (2024) described a methodology for identifying the most efficient control mechanism for a new controller. Their study provides a clear resolution to the Karush–Kuhn–Tucker problem and simplifies computations to reduce complexity. However, it still requires numerous sensors and involves certain intricacies.

Sozanski and Szczesniak (2023) presented a novel approach for controlling a shunt APF using the sliding discrete Fourier transform (SDFT) technique. This method leverages the conventional SDFT algorithm while innovatively switching between two parallel SDFT algorithms. Although this technique requires a substantial number of mathematical operations, it can still be implemented using readily available microcontrollers.

Intelligent current techniques (ICT) rely on expert knowledge to extract information from signal processing (Boopathi and Indragandhi, 2023; Chen et al., 2022). To enhance the performance of APF for harmonic compensation, Hou et al. (2024) proposed a control strategy for APF reference compensation current based on a Recurrent Wavelet Fuzzy Neural Network (RWFNN). Implementing ICT requires a deep understanding of the functional and behavioural aspects of APF systems.

Linear controllers, such as proportional-integral (PI) controllers, are frequently used to regulate the current loop of an LCL GTI (Cha et al., 2009; Kolek and Firlit, 2021). These controllers are widely adopted due to their simplicity and effectiveness. However, they come with limitations, notably instability issues and challenges in reference tracking (Trinh and Lee, 2012). Proportional-resonant (PR) controllers offer significant improvements in reference tracking and can address some shortcomings of conventional PI controllers (Alathamneh et al., 2022; Kolek and Firlit, 2021). However, PR controllers only compensate for a single frequency (Avci and Ucar, 2020; Trinh and Lee, 2012). To overcome these limitations, proportional multi-resonant (PMR) controllers are employed. A PMR controller combines a proportional controller, a resonant controller tuned to the fundamental frequency and additional resonant controller to mitigate all harmonics, including those caused by non-linear loads (Hao et al., 2012; Utkin, 1978). Non-linear controllers, particularly sliding mode controllers (SMCs), exhibit desirable characteristics such as fast dynamic response and robustness to parameter variations when compared to conventional controllers (Guzman et al., 2016; Huang et al., 2019; Rabbani et al., 2023). The sliding surface of the LCL GTI typically involves a linear combination of variables encompassing the inverter current error, capacitor voltage error, grid current error and their respective integrals or derivatives (Altin et al., 2018; Ammar et al., 2024; Boukattaya et al., 2018).

In this study, an SMC strategy in the natural frame is introduced for a three-phase grid-tied system with LCL filters. The derivation of the sliding surface function is based on the error of the capacitor voltage and its derivative. Due to the inherent active damping effect of capacitor voltage measurement on the system, resonance damping occurs automatically, eliminating the need for a virtual resistor in the closed-loop system. The generation of the capacitor voltage reference is facilitated by a PMR controller, ensuring zero steady-state error in both the fundamental and harmonic components of the grid current. Furthermore, an interconnected non-linear load is linked to the grid, enabling the inverter to function as an APF. The primary advantage of this methodology is its intrinsic ability to

achieve sinusoidal grid currents with low total harmonic distortion (THD) without the necessity of compensating for grid harmonics to obtain a sine wave output with minimal harmonic distortion (Hao et al., 2012). The novelties of the proposed method are as follows:

- Developing NFTSMC for controlling a three-phase GTI with an LCL filter, demonstrating the suitability of NFTSMC for systems with inherent uncertainties and external disturbances, and ensuring robust and precise control.
- Combining NFTSMC with a PMR controller to ensure both robust dynamics and zero steady-state error in grid currents.
- Reducing susceptibility to parameter uncertainties, particularly regarding fluctuations in grid inductances.
- Mitigating phase discrepancies between the injected grid current and its reference value, especially in scenarios with lower APF ratings.
- Simplifying implementation by controlling the grid-side current rather than the inverter-side current.
- Providing rapid dynamic response and precise tracking capabilities of the NFTSMC under step changes and varying operating conditions.
- Unlike traditional SMC, the NFTSMC approach avoids singularities and chattering, making it suitable for real-world APFs with lower computational complexity.

The rest of the paper is organised as follows. Section 2 presents a brief modelling of the GTI with LCL filter. The NFTSMC and PMR controllers are introduced and designed in Sections 3 and 4. Simulation results are discussed in Section 5, and the paper is concluded in Section 6.

## 2. State-Space Modelling of GTI with LCL Filter

Figure 1 illustrates the configuration of a three-phase VSI equipped with an LCL filter. The LCL filter consists of the inverter-side inductor  $L_1$ , the filter capacitor  $C$  and the grid-side inductor  $L_2$ . The resistances  $r_1$  and  $r_2$  represent the parasitic series resistances of the inductors  $L_1$  and  $L_2$ , respectively. The VSI comprises six switching devices, which are governed by a controller-generated signal. The state-space equations for the VSI can be derived from the circuit as shown below:

$$L_1 \frac{di_1}{dt} + r_1 i_1 = \Gamma u_k V_{dc} - v_c, \quad (1)$$

$$L_2 \frac{di_2}{dt} + r_2 i_2 = v_c - v_{gk}, \quad (2)$$

$$C \frac{dv_c}{dt} = i_1 - i_2. \quad (3)$$

where  $\Gamma = \begin{bmatrix} 2 & -1 & -1 \\ -1 & 2 & -1 \\ -1 & -1 & 2 \end{bmatrix}$ ,  $i_1 = [i_{1a} \ i_{1b} \ i_{1c}]^T$ ,  $i_2 = [i_{2a} \ i_{2b} \ i_{2c}]^T$ ,  $v_c = [v_{ca} \ v_{cb} \ v_{cc}]^T$  and  $v_{gk} = V_g \cos(\omega t + \varphi_k)$  with  $\varphi_k$  takes

0,  $-2\pi/3$  and  $-4\pi/3$  for phases a, b and c, respectively.  $u_k$  is the bipolar switching function defined as

$$u_k = \begin{cases} 1, & \text{upper q closed} \\ -1, & \text{lower q closed} \end{cases} \quad \text{and } k = a, b, c \quad (4)$$

and the reference current  $i_{2,k}^*$ , which consist of reference current ( $i_{2s,k}^*$ ) and harmonic detected current of non-linear load ( $i_{lh,k}$ ), is defined as

$$i_{2,k}^* = i_{2s,k}^* + i_{lh,k} = I_2^* \cos(\omega t + \varphi_k + \theta) + i_{lh,k} \quad (5)$$

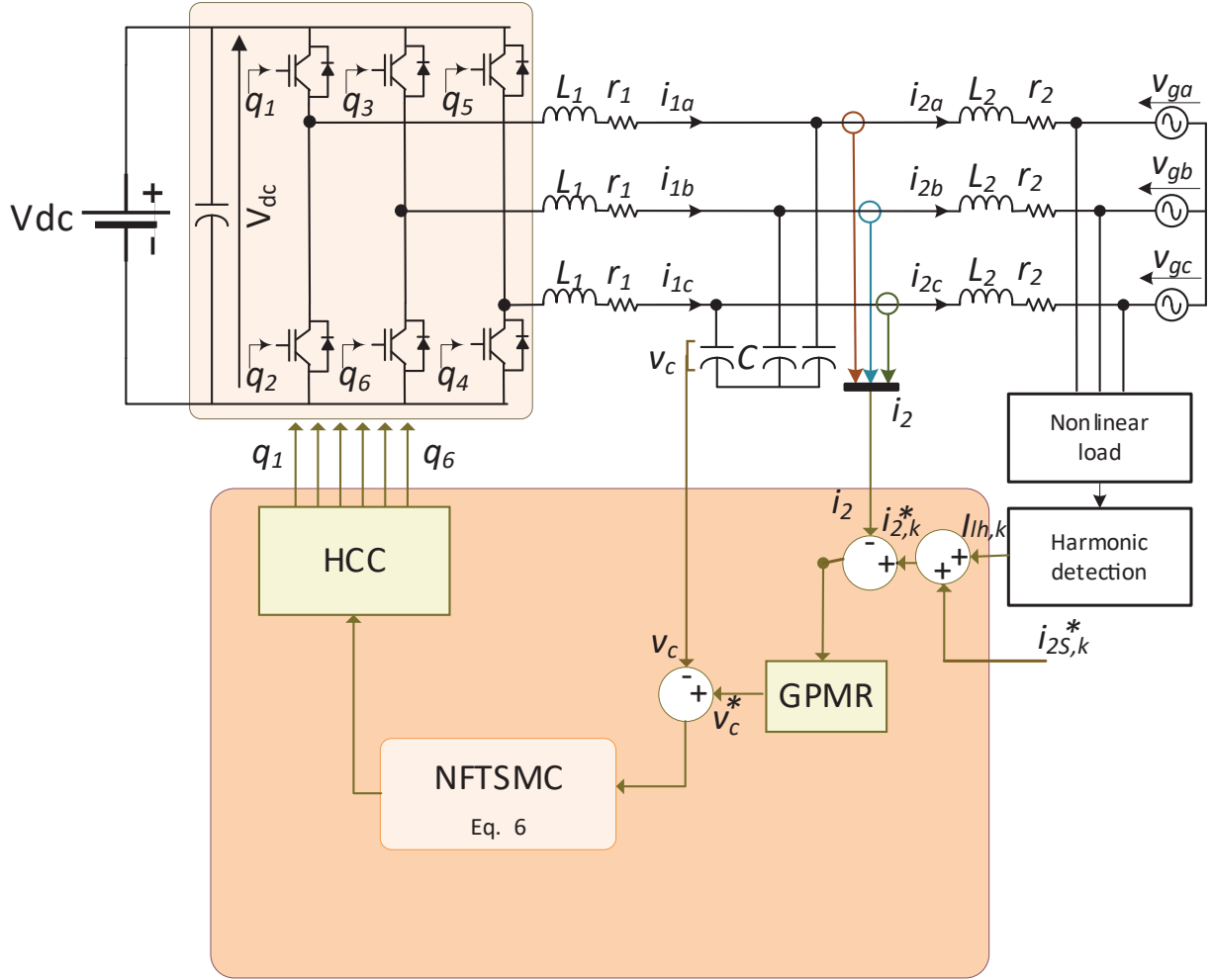


**Figure 1.** Three-phase LCL-filtered GTI with the proposed control scheme. GTI, grid-tied inverter; HCC, hysteresis current controller.

### 3. Proposed Non-Singular Fast Terminal Sliding Mode Controller (NFTSMC)

It should be noted that the generation of  $v_c^*$  is performed by PMR and will be discussed in Section 4.

The sliding surface function vector can be defined as (Zhang and Fei, 2023)

$$S = x_1 + k_1 |x_1|^\alpha \text{sign}(x_1) + k_2 |x_2|^\beta \text{sign}(x_2) \quad (6)$$

where  $k_1$  and  $k_2$  are positive constants  $1 < \beta < 2$  and  $\beta < \alpha$ .  $x_1$  and  $x_2$  are calculated by Eqs (7) and (8)

$$x_1 = v_c^* - v_c \quad (7)$$

$$x_2 = \dot{v}_c^* - \dot{v}_c \quad (8)$$

During the sliding regime, the dynamics of the converter are forced to slide along the sliding surface. To design an effective SMC system, it is necessary to satisfy the following condition (Bacha et al., 2014).

$$S\dot{S} < 0 \quad (9)$$

where  $\dot{S}$  is the time derivative of  $S$  and it is presented in Eq. (10).

$$\dot{S} = x_2 + \alpha k_1 |x_1|^{\alpha-1} x_2 + \beta k_2 |x_2|^{\beta-1} \dot{x}_2 \quad (10)$$

According to Eqs (7) and (8), the derivative of  $x_1$  can be obtained

$$\dot{x}_1 = x_2 \quad (11)$$

By substitution Eq. (3) into Eq. (8) gives us

$$x_2 = \frac{dv_c^*}{dt} - \frac{dv_c}{dt} = \frac{dv_c^*}{dt} - \frac{1}{C} [i_1 - i_2] \quad (12)$$

Taking a derivative of Eq. (12) results in

$$\dot{x}_2 = \frac{d^2 v_c^*}{dt^2} - \frac{1}{C} \left( \frac{di_1}{dt} - \frac{di_2}{dt} \right) \quad (13)$$

Substituting  $\frac{di_1}{dt}$  and  $\frac{di_2}{dt}$  from Eqs (1) and (2) in Eq. (13) yields

$$\dot{x}_2 = \frac{d^2 v_c^*}{dt^2} - \frac{1}{L_1 C} u V_{dc} + \frac{1}{L_1 C} v_c + \frac{r_1}{L_1 C} i_1 + \frac{1}{L_2 C} v_c - \frac{1}{L_2 C} v_g - \frac{r_2}{L_2 C} i_2 \quad (14)$$

Now, substituting  $i_1$  instead of  $i_2 + C dv_c/dt$  yields

$$\dot{x}_2 = \frac{d^2 v_c^*}{dt^2} - \frac{1}{L_1 C} u V_{dc} + \frac{1}{L_1 C} v_c + \frac{r_1}{L_1 C} i_2 + \frac{r_1}{L_1} \frac{dv_c}{dt} + \frac{1}{L_2 C} v_c - \frac{1}{L_2 C} v_g - \frac{r_2}{L_2 C} i_2 \quad (15)$$

By replacing  $dv_c/dt$  with  $dv_c^*/dt - x_2$  and adding the terms  $\frac{1}{L_1 C} v_c^* - \frac{1}{L_1 C} v_c^*$  and  $\frac{1}{L_1 C} v_c^* - \frac{1}{L_1 C} v_c^*$  into Eq. (15), we finally obtain

$$\dot{x}_2 = \omega_1^2 u V_{dc} - \omega_r^2 x_1 - \frac{r_1}{L_1} x_2 + D \quad (16)$$

where  $\omega_1 = 1/\sqrt{L_1 C}$ ,  $\omega_2 = 1/\sqrt{L_2 C}$ ,  $\omega_r = \sqrt{(L_1 + L_2)/L_1 L_2 C}$  and  $D$  is disturbance term which can be obtained from

$$D = r_1 \omega_1^2 i_2 - r_2 \omega_2^2 i_2 + \frac{d^2 v_c^*}{dt^2} + \frac{r_1}{L_1} \frac{dv_c^*}{dt} + \omega_r^2 v_c^* - \omega_2^2 v_g \quad (17)$$

Substitution of Eqs (12) and (17) in Eq. (10) results in

$$\dot{S} = \left( 1 + \alpha k_1 |x_1|^{\alpha-1} - \frac{r_1}{L_1} \beta k_2 |x_2|^{\beta-1} \right) x_2 + \beta k_2 |x_2|^{\beta-1} \left( \omega_1^2 u V_{dc} - \omega_r^2 x_1 + D \right) \quad (18)$$

Now, defining the control variable

$$u = -\text{sign}(S) \quad (19)$$

By Eqs (19) and (18) existing condition obtained

$$\dot{S} = \left( 1 + \alpha k_1 |x_1|^{\alpha-1} - \frac{r_1}{L_1} \beta k_2 |x_2|^{\beta-1} \right) x_2 + \beta k_2 |x_2|^{\beta-1} \left( \omega_1^2 u V_{dc} - \omega_r^2 x_1 + D \right) \quad (20)$$

(1) When  $S < 0 \rightarrow u = 1$ ;

$$\left(1 + \alpha k_1 |x_1|^{\alpha-1} - \frac{r_1}{L_1} \beta k_2 |x_2|^{\beta-1}\right) x_2 + \beta k_2 |x_2|^{\beta-1} (\omega_1^2 V_{dc} - \omega_r^2 x_1 + D) > 0 \quad (21)$$

(2) When  $S > 0 \rightarrow u = -1$ ;

$$\left(1 + \alpha k_1 |x_1|^{\alpha-1} - \frac{r_1}{L_1} \beta k_2 |x_2|^{\beta-1}\right) x_2 + \beta k_2 |x_2|^{\beta-1} (D - \omega_1^2 V_{dc} - \omega_r^2 x_1) < 0 \quad (22)$$

The above inequality assures that the state variables remain on the sliding surface while converging towards the origin. During the sliding motion ( $S = 0$  and  $\dot{S} = 0$ ), Eqs (21) and (22) define the operational boundaries of the SMC system.

To mitigate the adverse effects of high-frequency switching and enhance the efficacy of the SMC, a sign function was employed as a replacement for the hysteresis function.

$$u = \begin{cases} 1, S < +h \\ -1, S > h \end{cases} \quad (23)$$

where  $+h$  and  $-h$  are the higher and lower bands of the hysteresis function.

The stability of the proposed reaching law can be evaluated using Lyapunov's stability criterion. For this purpose, the following function  $V$  is defined as the Lyapunov function:

$$V = 0.5 S^2 < 0 \quad (24)$$

By differentiating  $V$  with respect to time and applying Eq. (10), the following results are obtained.

$$\dot{V} = S\dot{S} = S \left( x_2 + \alpha k_1 |x_1|^{\alpha-1} x_2 + \beta k_2 |x_2|^{\beta-1} \dot{x}_2 \right) \quad (25)$$

Assuming that the state variables approach zero ( $x_{1a} \equiv x_{2a} \equiv 0$ ) during the sliding mode operation, the derivative of the sliding surface function for a phase can be expressed as follows:

$$\dot{S}_a \cong \frac{\omega_1^2 V_s}{6} (2u_a - u_b - u_c) + D_a \quad (26)$$

with

$$D_a = \frac{d^2 v_{ca}^*}{dt^2} + \frac{r_1}{L_1} \frac{dv_{ca}^*}{dt} + \omega_r^2 v_{ca}^* + (r_1 \omega_1^2 - r_2 \omega_2^2) i_{2sa}^* - \omega_2^2 v_{ga} \quad (27)$$

The voltage of the reference capacitor can be determined using the equations  $v_{ga} = V_g \cos \omega t$ , as indicated in Eqs (5) and (2), as follows.

$$v_{ca}^* = -\omega L_2 I_2^* \sin \omega t + (r_2 I_2^* + V_g \cos \omega t) \quad (28)$$

By substituting the undistorted grid voltage equation  $v_{ga} = V_g \cos \omega t$  and Eqs (5) and (27) into Eq. (26), the following outcome is obtained.

$$D_a = M_{1a} \sin \omega t + M_{2a} \cos \omega t = M_{da} \sin(\omega t + \gamma) \quad (29)$$

where

$$M_{1a} = \omega I_2^* \left( \omega^2 L_2 - \omega_r^2 L_2 - \frac{r_1 r_2}{L_1} \right) - \frac{\omega r_1}{L_1} V_g \quad (30)$$

$$M_{2a} = I_2^* \left( \omega_1^2 r_1 + \omega_1^2 r_2 - \omega^2 r_2 - \frac{\omega^2 r_1 L_2}{L_1} \right) - V_g (\omega^2 - \omega_1^2) \quad (31)$$

$$M_{da} = \sqrt{M_{1a}^2 + M_{2a}^2}, \gamma = \tan^{-1} \left( \frac{M_{2a}}{M_{1a}} \right) \quad (32)$$

Substituting Eqs (21) and (26) into Eq. (24) result in

$$S_a \left[ \frac{\omega_1^2 V_s}{3} \text{sign}(S_a) - \frac{\omega_1^2 V_s}{6} \text{sign}(S_b) - \frac{\omega_1^2 V_s}{6} \text{sign}(S_c) - D_a \right] < 0 \quad (33)$$

Assuming  $S_b > 0$  and  $S_c < 0$  and utilising the equations  $|S_a| = S_a \text{sign}(S_a)$  and  $S_a = |S_a| \text{sign}(S_a)$ , we derive the following results

$$\frac{1}{3} |S_a| [\omega_1^2 V_s - \text{sign}(3D)] < 0 \quad (34)$$

The inequality in Eq. (34) is valid provided that the subsequent condition is met

$$|3D_a| > \omega_1^2 V_s \quad (35)$$

Eq. (35) can be stated as

$$-\omega_1^2 V_s < 3D_a < \omega_1^2 V_s \quad (36)$$

Now, dividing both sides by  $\omega_1^2 V_s$  gives

$$-1 < \frac{3D_a}{\omega_1^2 V_s} < 1 \quad (37)$$

Substituting Eq. (29) into Eq. (37) and using  $\gamma \cong -90^\circ$  gives

$$-1 < \frac{3M_{da}}{\omega_1^2 V_s} \cos \omega t < 1 \quad (38)$$

By substituting the parameters utilised in the simulation study, it is observed that the condition expressed in Eq. (38) is consistently satisfied within the interval where  $S_b > 0$  and  $S_c < 0$ . Furthermore, the analogous control for the remaining legs can be derived through a similar approach.

## 4. Generation of Capacitor Voltage Reference by PMR Controller

Following the development of the inner loop controller, the PMR-based outer current loop is evaluated for its capability to compensate for low-order harmonics. This approach simplifies the controller design and reduces the computational burden within the inverter system, as it avoids the need for axis transformations or non-linear control

strategies. The PMR controller generates  $v_c^*$ , ensuring zero steady-state error in the grid current. When the network current error ( $i_2^* - i_2$ ) is applied to the input of the PMR controller, the output  $v_c^*$  is obtained, ensuring that  $i_2$  follows  $i_{2s,k}^* + i_{lh,k}^*$ .

The transfer function of the PR controller ( $G_{PR}(s)$ ) is defined in Eq. (39), where  $K_p$ ,  $K_i$ ,  $w_0$  and  $w_c$  denote the proportional part, resonant gain, fundamental frequency and cut-off frequency of the PR controller, respectively. Although  $G_{PR}(s)$  exhibits high gain exclusively at the fundamental frequency, it can be expanded to address multiple low-order harmonics ( $h$ ) as shown in Eq. (40). Here,  $K_p$  represents the proportional part of the PMR controller, and  $h$  signifies the harmonic order where the frequency determines the PMR controller's resonant frequency ( $w_h$ ). By employing the PMR controller, each harmonic component in the output current can be effectively and individually suppressed, achieving zero steady-state error.

$$G_{PR}(s) = K_p + \frac{2K_i\omega_c S}{S^2 + 2\omega_c S + \omega_0^2} \quad (39)$$

$$G_{PMR}(s) = K_p + \sum_{h=1,5,7,9} \frac{2K_i\omega_{ch} S}{S^2 + 2\omega_{ch} S + \omega_h^2} \quad (40)$$

## 5. Simulation Results

The validation of the system, as illustrated in Figure 1, was performed through simulation using the parameters specified in Table 1. A Hysteresis current controller (HCC) was employed for this purpose, with the simulation carried out in Matlab/Simulink (The MathWorks, Inc., Natick, MA, USA). The objective of this study is to evaluate the performance of a control structure in which a dependent current source is utilised as a non-linear load. The  $G_{PMR}$  block, which represents the PMR controller, is used to generate the reference for the capacitor voltage.

Figure 2 illustrates the steady-state performance of the proposed system under a highly non-linear load. The grid current and voltage maintain consistent phase alignment, demonstrating the system's stability. Additionally, the LCL filter effectively suppresses switching harmonics, with no resonance observed in the grid current.

To evaluate the tracking capability of the controller, a step change was applied to the current reference value, and the results are shown in Figure 3. Specifically, at  $t = 0.1$  s, the current set point was increased by 100% from its initial peak value of 20 A to 40 A. The results depicted in Figure 3 highlight the controller's rapid response and its ability to track the reference value accurately with short settling time.

The resilience of the proposed model against parameter variations was also assessed through simulations with altered grid-side inductance values: a 20% decrease (0.549 mH) and a 500% increase (3.433 mH). The outcomes presented in Figure 4 confirm the robustness of the model under both increased and decreased inductance conditions. Notably, THD of the grid current was measured at 0.33% and 0.53% for the cases shown in

**Table 1.** System parameters

System parameter	Symbol	Value
DC link voltage	$V_d$	600 V
Grid voltage	$V_g$	230 V (RMS)
Grid frequency	$f_g$	50 Hz
Sampling rate		0.2 $\mu$ s
Inverter-side inductance	$L_1$	1.74 mH
Grid-side inductance	$L_2$	0.68 mH
Filter capacitance	$C$	10 $\mu$ F
Inductor's resistance	$r_{1,2}$	0.2 $\Omega$
Coefficient of NFTSMC	$\alpha, \beta, k_1, k_2$	1.8, 1.3, 300, 1
PMR gains	$K_p, K_i, k_s, k_7$	10, 2,000, 2,000, 2,000
Bands of the hysteresis function	$h$	2,000

PMR, proportional multi-resonant.



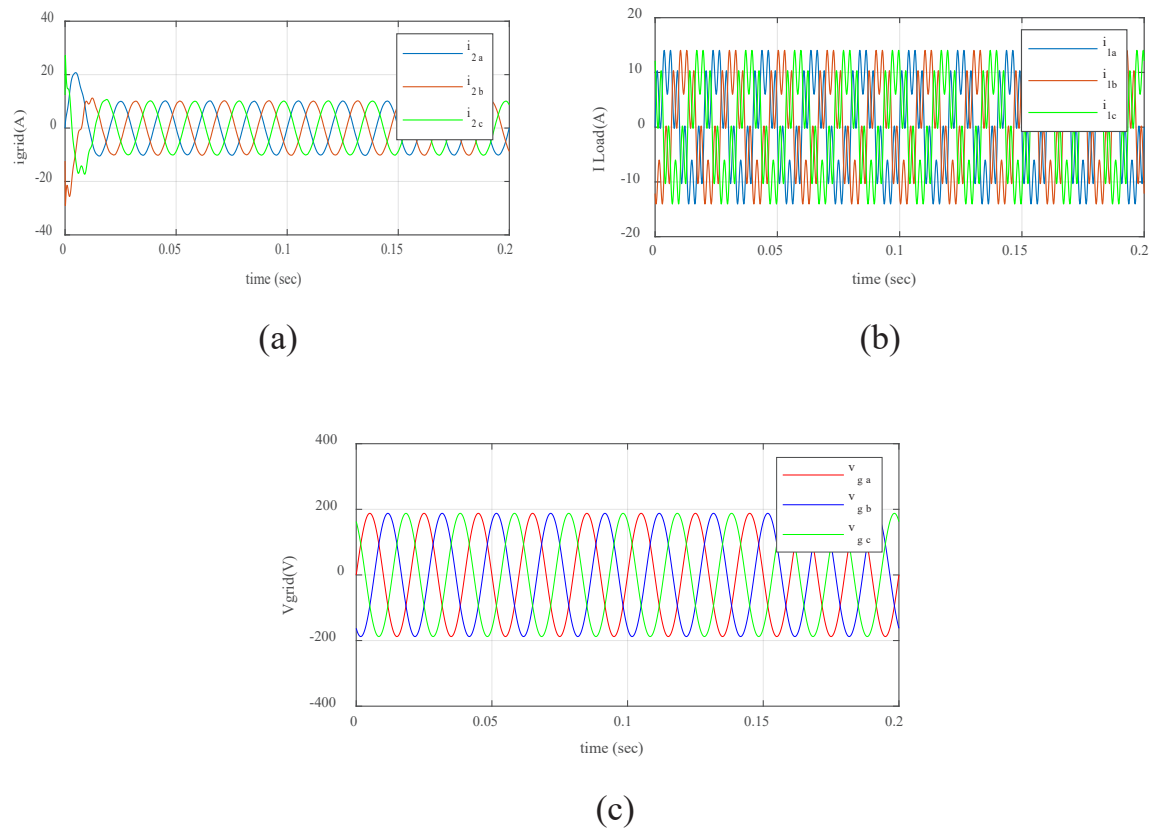


**Figure 2.** Steady-state waveforms of GTI (a) grid current ( $i_{2a}$ ,  $i_{2b}$ ,  $i_{2c}$ ) (b) load current ( $i_{la}$ ,  $i_{lb}$ ,  $i_{lc}$ ) (c) grid voltage ( $v_{ga}$ ,  $v_{gb}$ ,  $v_{gc}$ ). GTI, grid-tied inverter.

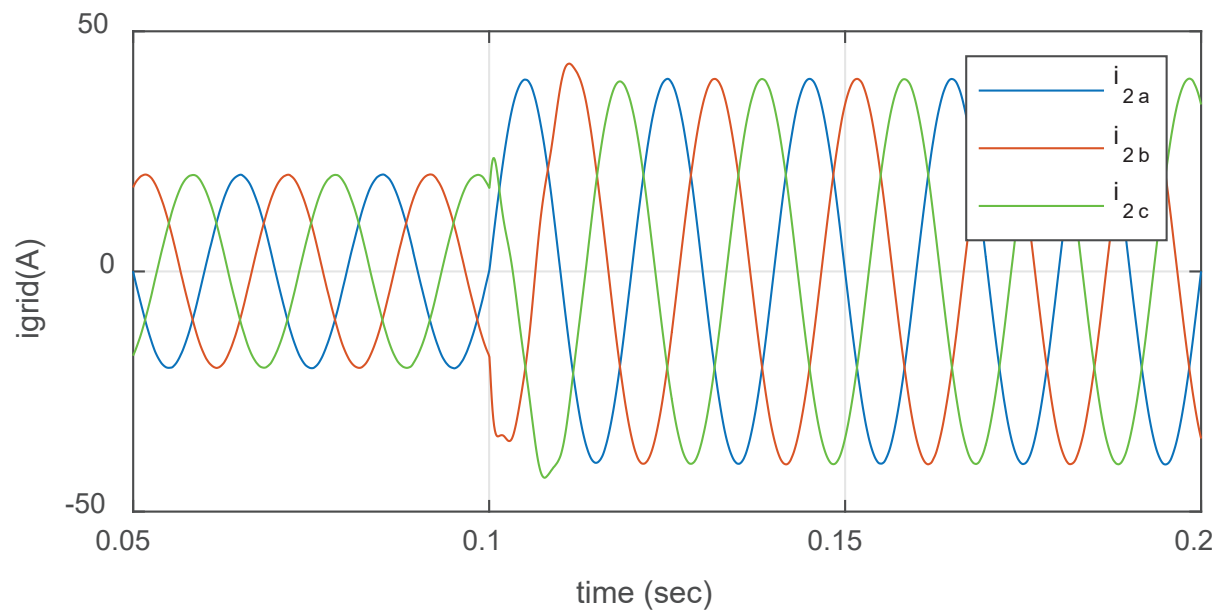


**Figure 3.** Grid current ( $i_{2a}$ ,  $i_{2b}$ ,  $i_{2c}$ ) responses to the variation of reference grid current.

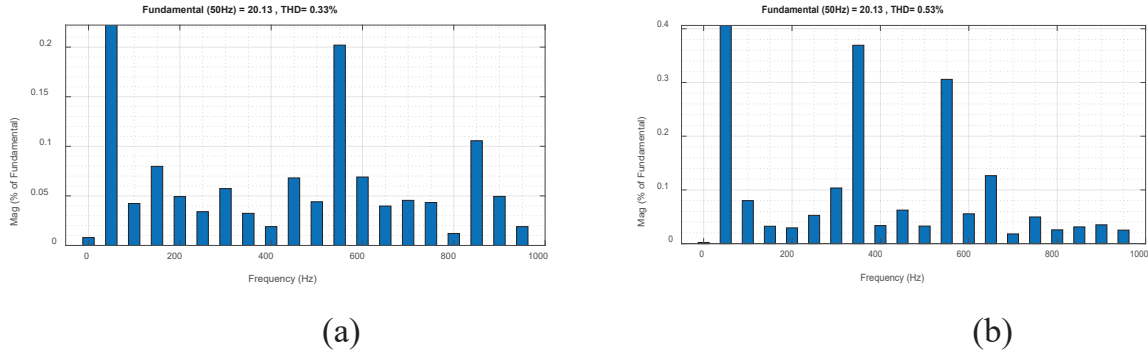


**Figure 4.** Fast Fourier transform of Grid-side current ( $i_{2a}$ ) for two different values of L2: (a) 20% decrease and (b) 500% increase. THD, total harmonic distortion.

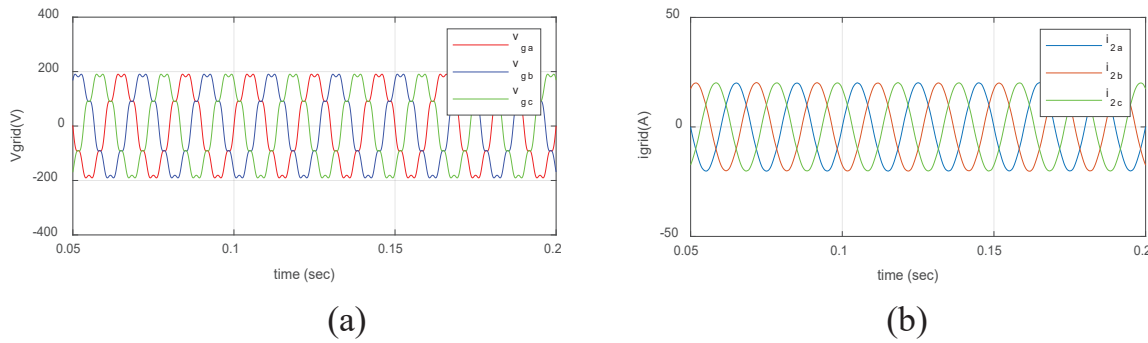


**Figure 5.** Simulation results under distorted grid voltage conditions: (a) grid voltage (b) grid current.

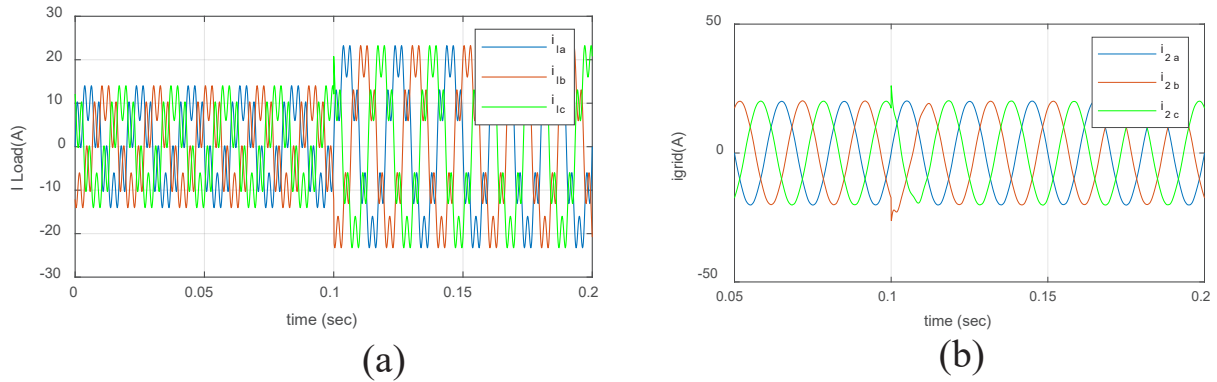


**Figure 6.** Load step change at  $t = 0.1$  s. (a) load current ( $i_{1a}$ ,  $i_{1b}$ ,  $i_{1c}$ ) and (b) grid current ( $i_{2a}$ ,  $i_{2b}$ ,  $i_{2c}$ ).

Figures 4(a) and 4(b), respectively. These values remain well within the IEEE standard limits (<5%), demonstrating the system's robustness and ability to maintain performance despite significant deviations in inductance.

The proposed controller is capable of functioning reliably even when the grid voltage is distorted. The performance of the VSI under such conditions is illustrated in Figure 5. It is noteworthy that a dedicated PLL (phase-locked loop) algorithm for extracting positive and negative sequence grid voltage components is not a prerequisite in this scenario. The THD recorded was 0.86%, which is still compliant with the criteria outlined in IEEE Std 519-2014. These results demonstrate the resilience and dependability of the proposed controller, rendering it suitable for deployment in diverse applications where grid voltage balance cannot be guaranteed.

The three-phase grid currents ( $i_{2a}$ ,  $i_{2b}$ ,  $i_{2c}$ ) and the load current variation following compensation are depicted in Figure 6. The results demonstrate the effectiveness of the controller, as evidenced by the grid currents maintaining

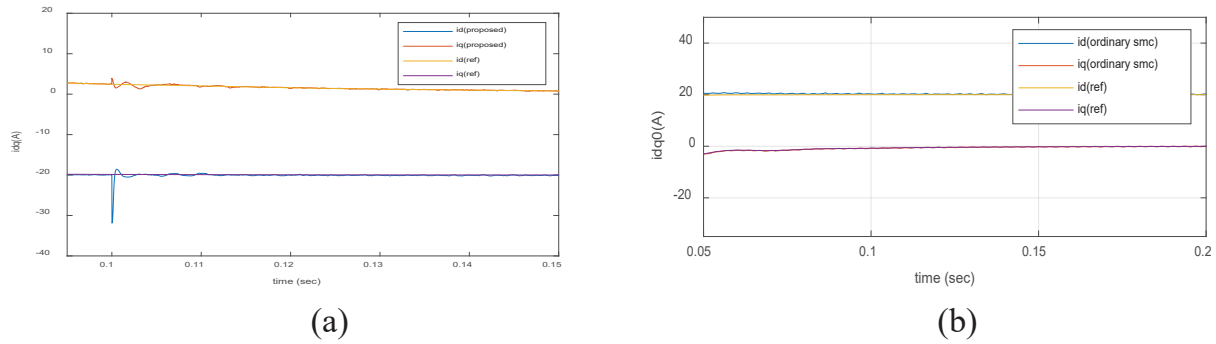


**Figure 7.** Comparison of the proposed NTFSMC with ordinary SMC under step change. SMC, sliding mode controller.

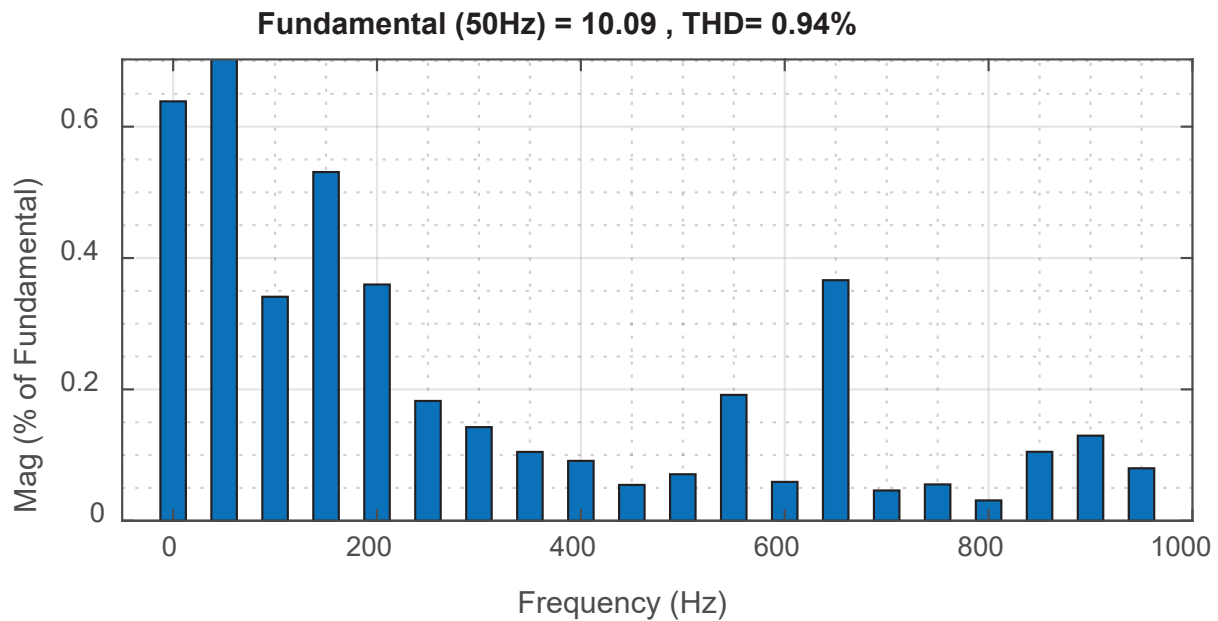


**Figure 8.** Fast Fourier transform of grid-side current ( $i_{2a}$ ) for Non-ideal DC voltage. THD, total harmonic distortion.

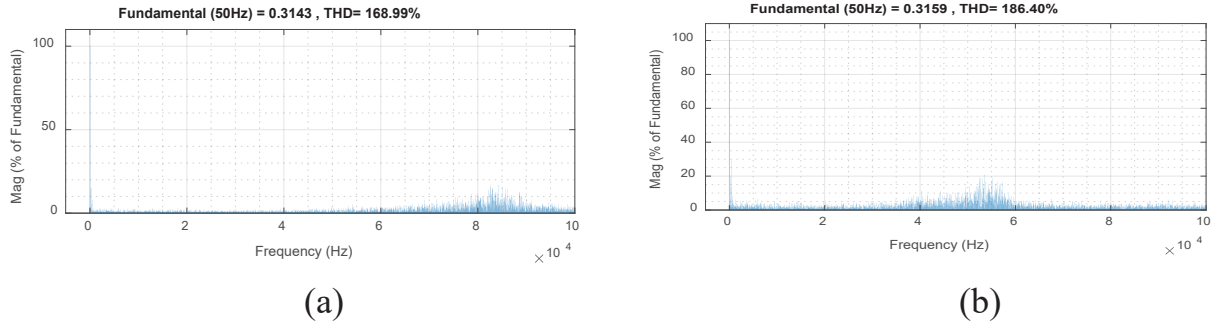
a sinusoidal waveform even under significant changes in load conditions. Notably, at  $t = 0.1$  s, the current of the non-linear load experiences a two-fold increase. Despite this abrupt and substantial rise in load current, the grid currents remain unaffected in terms of waveform distortion.

Figure 7 compares the dynamic performance of the NFTSMC with that of conventional SMC. The results reveal that NFTSMC exhibits a faster dynamic response, enabling the system to reach the desired values more quickly, under sudden load changes or step inputs. Additionally, NFTSMC achieves lower steady-state error due to its design, which eliminates chattering, a common issue in traditional SMC, and ensures smoother control actions. Furthermore, the results indicate enhanced precision in current tracking within the dq frame.

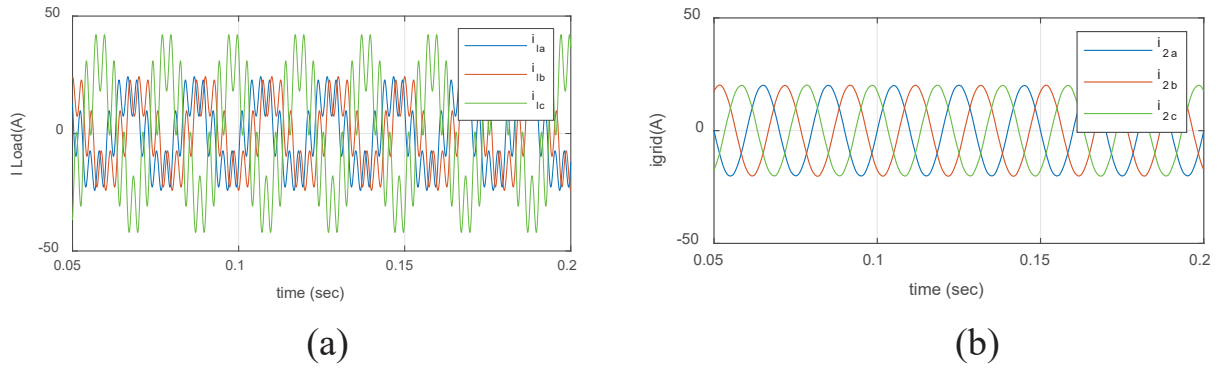
Figure 8 illustrates the fast Fourier transform of the grid-side current ( $i_2$ ) when DC voltage is series with 60- $\Omega$  resistor. This demonstrates that the system operates effectively, even in the presence of non-ideal DC voltage conditions.

Figure 9 illustrates that an increase in the hysteresis band results in a corresponding decrease in the switching frequency; however, the dynamic response remains unchanged within this domain. It is important to note that a reduction in frequency adversely affects the THD of the grid current ( $i_2$ ), increasing it from 0.66 to 2.49.

Moreover, the system exhibits robust performance when exposed to non-linear and non-symmetrical loads. The empirical evidence presented in Figure 10 confirms that the system functions adequately under these adverse conditions, achieving a THD of 1.14 in the grid current, which is indicative of a highly favourable outcome.



**Figure 9.** Fast Fourier transform switching pulses (a)  $h = 2,000$  (b)  $h = 1,000,000$ . THD, total harmonic distortion.



**Figure 10.** Non-symmetrical distortions in C phase. (a) non-symmetrical load and (b) sinusoidal grid current.

**Table 2.** Comparison of the proposed system with other works

Reference	Huang et al. (2023)	Zhang and Fei (2023)	Sozanski and Szczesniak (2023)	Proposed
Transient response performance	Very high	Very high	Medium	Very high
Robustness	High	High	High	Very high
PWM method	PWM	PWM	PWM	Hysteresis
Switching frequency	20 KHz	Not reported	25.6 KHz	Not fixed
Non-linear load performance	Very high	Very high	Very high	Very high
Complexity	High	High	High	Low
Computational burden	Very high	High	High	Low
Best grid THD	0.98	1.56	Not reported	0.33

THD, total harmonic distortion.

This study also includes a comparative analysis of the NFTSMC and PMR controlled system with other related methods, as summarised Table 2. While the modulation techniques described in Sozanski and Szczesniak (2023), Huang et al. (2023) and Zhang and Fei (2023) exhibit superior performance in certain aspects, the proposed method offers distinct advantages, such as reduced complexity and computational burden, alongside promising dynamic behaviour and robustness. Unlike the methods in Huang et al. (2023) and Zhang and Fei (2023), which requires an explicit model of the system for implementation, the proposed method operates without such a model. This characteristic enhances its resilience to disturbances, further solidifying its suitability for real-world applications.

## 6. Conclusion

This study introduces a novel control strategy for a three-phase grid-connected VSI with an LCL filter, leveraging an NFTSMC and a PMR approach. A key feature of the proposed control strategy is the generation of three-phase

reference capacitor voltages as a critical component. To eliminate the need for derivative operations through the use of the PMR controller. This design ensures that the system operates independently of grid inductance, thereby enhancing robustness and reliability. The proposed method effectively addresses the challenges posed by non-linear loads, significantly enhancing power quality by minimising THD and achieving rapid tracking of reference currents. Moreover, the absence of system modelling requirements simplifies implementation while ensuring dynamic performance and robustness. Simulation results validate the controller's ability to maintain sinusoidal grid currents and compensate for harmonic distortions under various operating conditions. The PMR controller's intrinsic active damping capability further enhances system stability, removing the need for additional passive components. This work resolves several challenges in APF design and lays a strong foundation for future advancements. Potential avenues for future research include:

- *Integration of intelligent control methods*: Explore the use of machine learning algorithms to optimise real-time performance and adaptability of APF in dynamic environments.
- *Interaction with renewable energy sources*: Investigate the compatibility and performance of the proposed system with different types of renewable energy sources such as solar and wind power.
- *Scalability analysis*: Evaluate the scalability of the controller for larger grid systems and its impact on overall grid stability and reliability.
- *Energy storage integration*: Incorporate energy storage systems, such as batteries or supercapacitors, to optimise energy management and enhance grid performance.

## References

- Alali, M. A. E., Shtessel, Y. B. and Barbot, J. P. (2019). Grid-Connected Shunt Active LCL Control via Continuous Sliding Modes. *IEEE/ASME Transactions on Mechatronics*, 24(2), pp. 729–740. doi: 10.1109/TMECH.2019.2896140
- Alathamneh, M., Ghanayem, H. and Nelms, R. M. (2022). Bidirectional Power Control for a Three-Phase Grid-Connected Inverter under Unbalanced Grid Conditions Using a Proportional-Resonant and a Modified Time-Domain Symmetrical Components Extraction Method. *Energies*, 15(24), p. 9564. doi: 10.3390/en15249564
- Altin, N., Ozdemir, S., Komurcugil, H. and Sefa, I. (2018). Sliding-Mode Control in Natural Frame with Reduced Number of Sensors for Three-Phase Grid-Tied LCL-Interfaced Inverters. *IEEE Transactions on Industrial Electronics*, 66(4), pp. 2903–2913. doi: 10.1109/TIE.2018.2847675
- Ammar, A., Belaroussi, O., Benakcha, M., Zemmit, A. and Ameid, T. (2024). Super-Twisting MRAS Observer-Based Non-linear Direct Flux and Torque Control for Induction Motor Drives. *Power Electronics and Drives*, 9, pp. 374–396. doi: 10.2478/pead-2024-0024
- Avci, E. and Ucar, M. (2020). Proportional Multi-Resonant-Based Controller Design Method Enhanced with a Lead Compensator for Stand-Alone Mode Three-Level Three-Phase Four-Leg Advanced T-NPC Inverter System. *IET Power Electronics*, 13(4), pp. 863–872. doi: 10.1049/iet-pel.2019.0765
- Bacha, S., Munteanu, I., & Bratcu, A. I. (2014). Power electronic converters: modeling and control (Vol. 4). London, UK: Springer.
- Boopathi, R. and Indragandhi, V. (2023). Control Techniques for Renewable Energy Integration with Shunt Active Filter: A Review. *International Journal of Ambient Energy*, 44(1), pp. 424–441. doi: 10.1080/01430750.2022.2128413
- Bosch, S., Staiger, J. and Steinhart, H. (2017). Predictive Current Control for an Active Power Filter with LCL-Filter. *IEEE Transactions on Industrial Electronics*, 65(6), pp. 4943–4952. doi: 10.1109/TIE.2017.2772176
- Boukattaya, M., Mezghani, N. and Damak, T. (2018). Adaptive Nonsingular Fast Terminal Sliding-Mode Control for the Tracking Problem of Uncertain Dynamical Systems. *ISA Transactions*, 77, pp. 1–19. doi: 10.1016/j.isatra.2018.04.007
- Cha, H., Vu, T. K. and Kim, J. E. (2009). Design and control of proportional-resonant controller based photovoltaic power conditioning system. *2009 IEEE Energy Conversion Congress and Exposition*. IEEE, pp. 2198–2205.
- Chen, C. I., Chen, Y. C. and Chen, C. H. (2022). Recurrent Wavelet Fuzzy Neural Network-Based Reference Compensation Current Control Strategy for Shunt Active Power Filter. *Energies*, 15(22), p. 8687. doi: 10.3390/en15228687
- Dehghani, M., Mardaneh, M. and Shafiei, M. H. (2020). Sliding mode control for load harmonics

- compensation and PV voltage regulation in a grid-tied inverter through a single-stage MPPT. *2020 28th Iranian Conference on Electrical Engineering (ICEE)*. IEEE, pp. 1–6.
- Guzman, R., de Vicuna, L. G., Morales, J., Castilla, M. and Miret, J. (2016). Model-Based Active Damping Control for Three-Phase Voltage Source Inverters with LCL Filter. *IEEE Transactions on Power Electronics*, 32(7), pp. 5637–5650. doi: 10.1109/TPEL.2016.2605858
- Hao, X., Yang, X., Liu, T., Huang, L. and Chen, W. (2012). A Sliding-Mode Controller with Multiresonant Sliding Surface for Single-Phase Grid-Connected VSI with an LCL Filter. *IEEE Transactions on Power Electronics*, 28(5), pp. 2259–2268. doi: 10.1109/TPEL.2012.2218133
- Hou, S., Qiu, Z., Chu, Y., Gao, J. and Fei, J. (2024). Hybrid Intelligent Control Using Hippocampus-Based Fuzzy Neural Networks for Active Power Filter. *IEEE Transactions on Power Electronics*, 39(12), pp. 15924–15942. doi: 10.1109/TPEL.2024.3449043
- Huang, M., Li, H., Wu, W. and Blaabjerg, F. (2019). Observer-Based Sliding Mode Control to Improve Stability of Three-Phase LCL-Filtered Grid-Connected VSIs. *Energies*, 12(8), p. 1421. doi: 10.3390/en12081421
- Huang, J., Zhao, Y., Wang, J. and Zhang, P. (2023). A Hybrid Active Damping Strategy for Improving the Adaptability of LCL Converter in Weak Grid. *Electronics*, 13(1), p. 144. doi: 10.3390/electronics13010144
- Kolek, K. and Firlit, A. (2021). A New Optimal Current Controller for a Three-Phase Shunt Active Power Filter Based on Karush–Kuhn–Tucker Conditions. *Energies*, 14(19), p. 6381. doi: 10.3390/en14196381
- Liu, T., Liu, J., Liu, Z. and Liu, Z. (2019). A Study of Virtual Resistor-Based Active Damping Alternatives for LCL Resonance in Grid-Connected Voltage Source Inverters. *IEEE Transactions on Power Electronics*, 35(1), pp. 247–262. doi: 10.1109/TPEL.2019.2911163
- Lorzadeh, I., Askarian Abyaneh, H., Savaghebi, M., Bakhshai, A. and Guerrero, J. M. (2016). Capacitor Current Feedback-Based Active Resonance Damping Strategies for Digitally-Controlled Inductive-Capacitive-Inductive-Filtered Grid-Connected Inverters. *Energies*, 9(8), p. 642. doi: 10.3390/en9080642
- Lou, Z., Li, P., Ma, K. and Teng, F. (2022). Harmonics and Interharmonics Detection Based on Synchrosqueezing Adaptive S-Transform. *Energies*, 15(13), p. 4539. doi: 10.3390/en15134539
- Maciążek, M. (2022). Active Power Filters and Power Quality. *Energies*, 15(22), p. 8483. doi: 10.3390/en15228483
- Mondal, B. and Karuppaswamy, A. (2024). A Non-Iterative Design Method for Output LCL Filter with RC Damping in Grid-Connected Inverters. *IEEE Transactions on Industrial Electronics*, 71(12), pp. 15768–15779. doi: 10.1109/TIE.2024.3387080
- Rabbani, A., Mardaneh, M., Jamshidpour, E. and Poure, P. (2023). Improved sliding mode control and active damping for LCL-filtered voltage source inverter connected to distorted grid. *2023 IEEE International Conference on Environment and Electrical Engineering and 2023 IEEE Industrial and Commercial Power Systems Europe (EEEIC/I&CPS Europe)*. IEEE, pp. 1–6.
- Satpathy, G. and De, D. (2024). A Novel Proportional Multi-Resonant Current Controller Strategy for Reduced DC Voltage Fed D-STATCOM with Internal LCL Resonance Damping. *Power Electronics and Drives*, 9(44), pp. 122–141. doi: 10.2478/pead-2024-0008
- Sozanski, K. and Szczesniak, P. (2023). Advanced Control Algorithm for Three-Phase Shunt Active Power Filter Using Sliding DFT. *Energies*, 16(3), p. 1453. doi: 10.3390/en16031453
- Teodorescu, R., Blaabjerg, F., Liserre, M. and Loh, P. C. (2006). Proportional-Resonant Controllers and Filters for Grid-Connected Voltage-Source Converters. *IEEE Proceedings - Electric Power Applications*, 153(5), pp. 750–762. doi: 10.1049/ip-epa:20060008
- Trinh, Q. N. and Lee, H. H. (2012). An Advanced Current Control Strategy for Three-Phase Shunt Active Power Filters. *IEEE Transactions on Industrial Electronics*, 60(12), pp. 5400–5410. doi: 10.1109/TIE.2012.2229677
- Utkin, V. I. (1978). Sliding Modes and Their Application in Variable Structure Systems. Moscow: MIR Publishers.
- Zhang, L. and Fei, J. (2023). Intelligent Complementary Terminal Sliding Mode Using Multiloop Neural Network for Active Power Filter. *IEEE Transactions on Power Electronics*, 38(8), pp. 9367–9383. doi: 10.1109/TPEL.2023.3266738
- Zheng, X., Qiu, K., Hou, L., Liu, Z. and Wang, C. (2018). Sliding-mode control for grid-connected inverter with a passive damped LCL filter. *2018 13th IEEE Conference on Industrial Electronics and Applications (ICIEA)*. IEEE, pp. 739–744.